

Present denudation rates at selected sections of the South African escarpment and the elevated continental interior based on cosmogenic ^{3}He and ^{21}Ne

A. Kounov

Department of Geological Sciences, University of Cape Town, 7701 Rondebosch, South Africa

Institute of Geology and Palaeontology, Basel University, 4056 Basel, Switzerland

email: a.kounov@unibas.ch

S. Niedermann

GeoForschungsZentrum Potsdam, Telegrafenberg, 14473 Potsdam, Germany

email : nied@gfz-potsdam.de

M. J. de Wit

AEON and Department of Geological Sciences, University of Cape Town, 7701 Rondebosch, South Africa

email: maarten@cigces.uct.ac.za

G. Viola

Geological Survey of Norway, 7491 Trondheim, Norway

email: giulio.viola@ngu.no

M. Andreoli

South African Nuclear Energy Corporation, PO Box 582, 0001 Pretoria, South Africa

School of Geosciences, University of the Witwatersrand, P Bag 3, 2050 Wits, South Africa

email: marco@necsa.co.za

J. Erzinger

GeoForschungsZentrum Potsdam, Telegrafenberg, 14473 Potsdam, Germany

email: erz@gfz-potsdam.de

© 2007 September Geological Society of South Africa

ABSTRACT

Measurements of cosmogenic ^{3}He and ^{21}Ne concentrations in dolerite and quartzite samples from selected sites across the South African coastal escarpment and the interior plateau provide valuable estimates of the short-term (*i.e.*, a few hundred thousand years) denudation rates. Present-day denudation rates at the summit of the escarpment and on the inland plateau are more than an order of magnitude lower than those in the Cretaceous. Values between 1.0 and 2.1 m/Ma obtained from resistant quartzite samples and between 1.5 and 3 m/Ma from dolerite sills suggest a strong lithology control on the erosion. The observed patterns of denudation across different landform sites on the high plateau and along its flanking escarpment suggest that the morphology of the sampling sites together with the local climate conditions have controlled the denudation processes.

Introduction

Since the break-up of Gondwana, Southern Africa has been surrounded by elevated passive margins flanked by a classic escarpment (King, 1951; 1967). The evolution of passive continental margins and their adjacent escarpments reflects the long-term interaction of tectonic and surface processes. It is now known that passive margin morphology is the result of positive and negative feedback between tectonic uplift and subsidence on the one hand and sedimentation and denudation on the other hand (Beaumont *et al.*, 2000).

Apatite fission track and cosmogenic nuclide studies along the escarpment-flanked continental margin of Southern Africa have recently revealed variable denudation rates for various morphological features of the passive margin, including its coastal plain, the

seaward-facing escarpment and the elevated inland plateau (*e.g.* Fleming *et al.*, 1999; Cockburn *et al.*, 2000; Brown *et al.*, 2000; Bierman and Caffee, 2001; Van der Wateren and Dunai, 2001; Brown *et al.*, 2002; Raab *et al.*, 2002; Bierman and Nichols, 2004; Tinker, 2005; Tinker *et al.*, in review; Kounov *et al.*, in review). These studies suggest that since the onset of the rifting phase, significant changes in denudation rates have occurred, in particular a substantial decrease when Cenozoic rates are compared to those for the Cretaceous. The high denudation rates during the Cretaceous are likely related to intense tectonic activity coupled with warm and humid climatic conditions, whereas the more arid climate that prevailed during the Quaternary and possibly throughout much of the Tertiary, and an apparent lack of significant uplift, were responsible for a remarkable subsequent decrease in the denudation

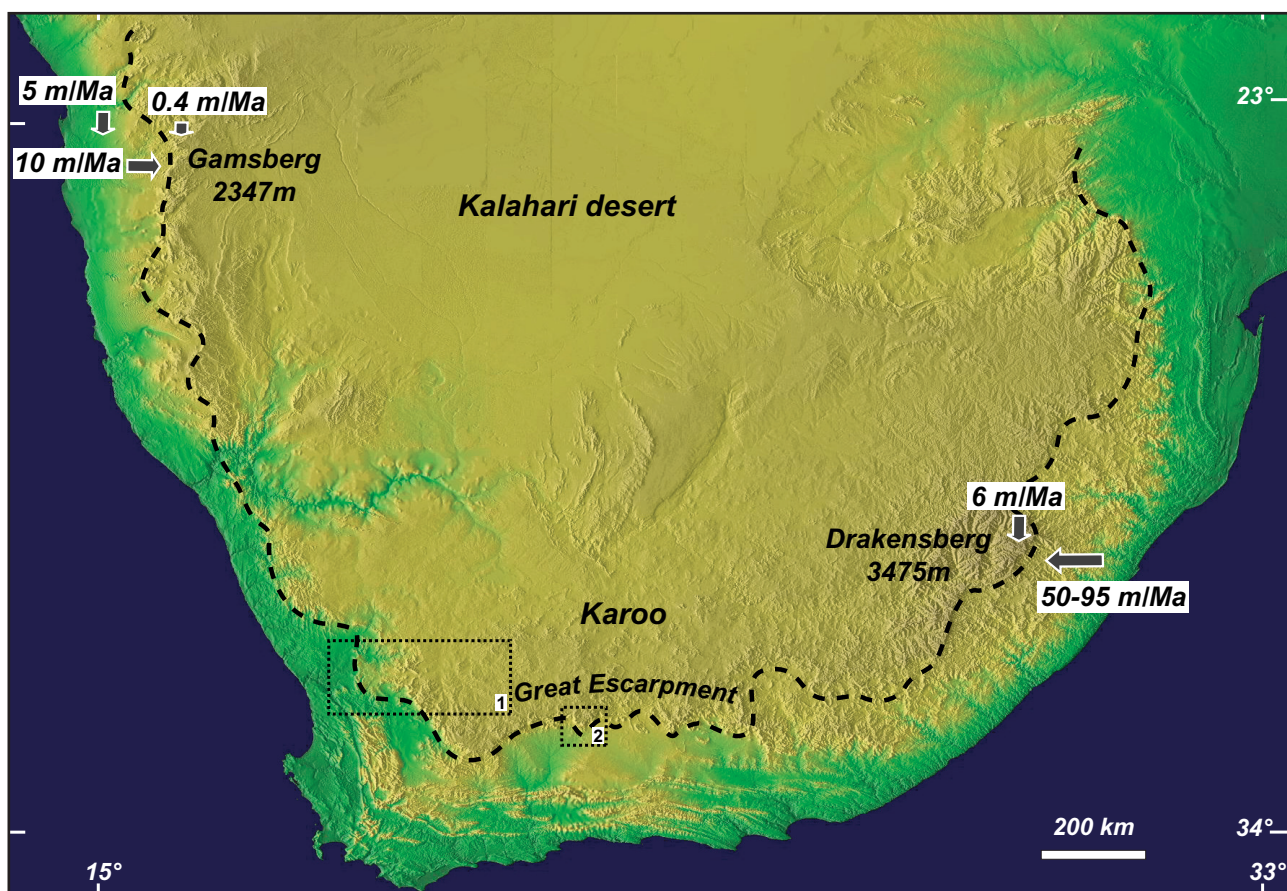


Figure 1. Shaded relief map of Southern Africa with previous cosmogenic nuclide results for denudation rate estimates from the Gamsberg (Cockburn *et al.*, 2000) and Drakensberg (Fleming *et al.*, 1999) escarpment areas. Boxes indicate site maps shown in Figures 2(a) (1) and 2(b) (2). The black dashed line represents the present-day position of the Great Escarpment.

rates (Brown *et al.*, 2000; 2002; Cockburn *et al.*, 2000; Tinker, 2005; Kounov *et al.*, in review).

One outstanding task related to the geomorphic evolution of South African landscape is a detailed account of the processes that affect its erosional sculpturing, and the recent evolution of these geomorphic features. To achieve this, we first need a firm understanding of present denudation rates, which will in turn enable us to compare them to those determined for the Cenozoic and Cretaceous.

Short-term (10^3 to 10^5 years) erosional processes and their rates can best be studied by applying in situ-produced cosmogenic nuclides, which reflect the particular conditions at a location much more specifically than other geochronological methods. Along the relatively dry west coast (Atlantic Ocean), Cockburn *et al.* (2000) reported cosmogenic ^{10}Be and ^{26}Al concentrations for siliciclastic rocks from the Gamsberg escarpment area in Namibia. Their results suggest a mean rate of horizontal escarpment retreat of ~ 10 m/Ma and vertical downwearing at its summit of 0.4 m/Ma, and a mean denudation rate of coastal inselbergs of ~ 5 m/Ma (Figure 1).

Along the relatively warm and humid east coast (Indian Ocean), significantly higher denudation rates were derived for basalts from the summit (6 m/Ma) and the free face (50 to 95 m/Ma) of the Drakensberg

escarpment, based on analyses of cosmogenic ^{36}Cl (Fleming *et al.*, 1999; Figure 1).

These results suggest significant differences in denudation rates for different regions along the Southern African margin that are likely to be predominantly related to local climatic differences and variations in the underlying geology.

Our study investigates further the interaction between climate, lithology and landscape formation. By means of cosmogenic ^{3}He and ^{21}Ne analysis we have constrained variations in denudation rates from different landform sites along the South African escarpment and the interior plateau. The selected sites represent stable surfaces underlain by different lithologies and characterised by different climatic conditions, offering an ideal opportunity to study in details the influence of both climate and lithology on the erosional agents that shape the present day topography. Moreover, our studies provide important information concerning the processes and the rates by which the elevated passive margins and in particular their main morphological features were formed.

In contrast to the relatively short-lived radionuclide ^{36}Cl ($T_{1/2} = 0.3$ Ma), the stable noble gas isotopes are ideally suited to study relatively long exposure histories (low denudation rates) in lithologies such as the Karoo dolerites, from which pyroxene phenocrysts can be

separated. Reliable measurements of the radionuclides ^{10}Be and ^{26}Al ($T_{1/2} = 1.5$ and 0.7 Ma, respectively), on the other hand, are at present only possible in quartz, where ^{21}Ne analyses have also been successfully applied (e.g. Niedermann, 2002). Since our study involves both pyroxene and quartz-bearing lithologies, the noble gases were chosen as an appropriate dating tool for our purposes.

Geological setting of sampling sites

Along the west coast, in the vicinity of Vanrhynspass, the escarpment is extremely well defined as an ~600 m sub-vertical scarp formed in Neoproterozoic sedimentary rocks of the Gariep and Nama Groups that consists mainly of shales and siltstones (Figure 2a; Tankard *et al.*, 1982). The summit of the escarpment is capped by an ~50 m layer of flat-lying quartzite-dominated lithologies of the Lower Palaeozoic Table Mountain Group (TMG;

Tankard *et al.*, 1982; Figure 2a) that disappears beneath their Karoo cover farther inland. Northwards, in the area of Knersvlakte (Figure 2a), the escarpment gradually becomes less distinct and in places completely disappears due to the primary thinning and finally pinch-out of the TMG cover. Thus the extent of the escarpment in this region appears to be lithologically controlled by the resistance to erosion of the quartzite cover.

Farther south-east, and down to the Drakensberg area, the escarpment coincides closely with the limit of the mid-Jurassic dolerite sills intruded into the sedimentary strata of the Upper Palaeozoic Karoo sequence (Tankard *et al.*, 1982). Near Beaufort West, about 200 km inland from the south coast, the escarpment has a relief of ~1800 m and generally coincides with a major drainage divide. From there north, the interior plateau retains a mean elevation of

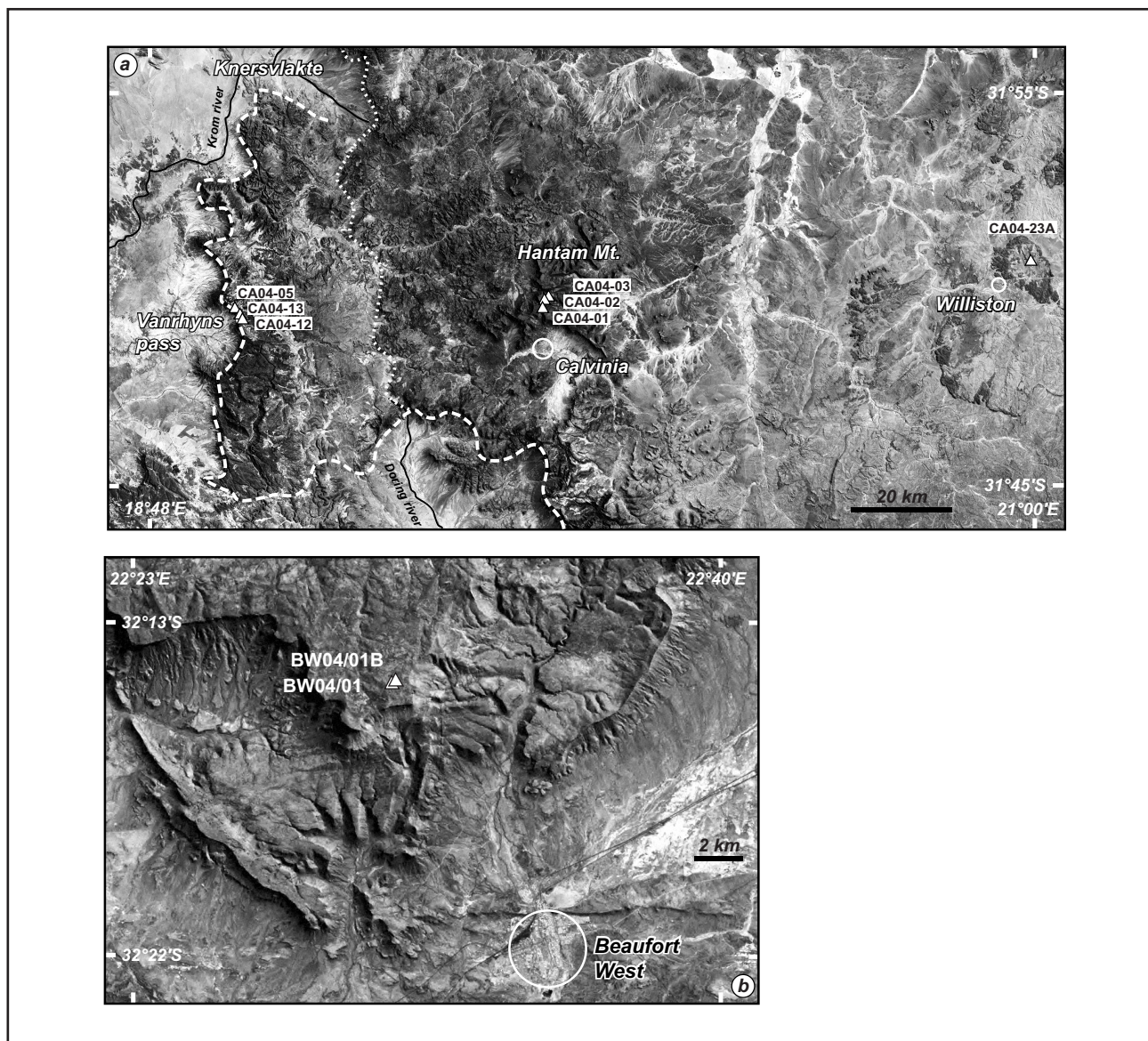


Figure 2. Landsat images of the studied areas with the location of the samples. (a) The area between Vanrhynspass and Williston. The thick dashed line represents the present-day position of the escarpment in the area; the thin dashed line shows the limit of the Karoo dolerite sills. (b) Escarpment area near Beaufort West.

Table 1. Information on samples used for the cosmogenic nuclide study. For more details see text and Figures 2–6.

Sample	Location	Mineral	Latitude [°S]	Longitude [°E]	Altitude [m]	Inclination
BW04/01	Beaufort West	px	32.254	22.505	1800	5°
BW04/01B	Beaufort West	px	32.254	22.505	1800	5°
CA04/01	Hantam Mt.	px	31.381	19.784	1520	0°
CA04/02A	Hantam Mt.	px	31.367	19.787	1500	7°
CA04/02B	Hantam Mt.	px	31.359	19.787	1500	0°
CA04/03	Hantam Mt.	px	31.35	19.794	1505	0°
CA04/05	Vanrhynspass	qz	31.373	19.017	831	0°
CA04/12	Vanrhynspass	qz	31.376	19.020	83	0°
CA04/13	Vanrhynspass	qz	31.375	19.019	828	30°
CA04/23A	Williston	px	31.287	20.991	1192	0°

~1000 m, with low relief. The top of the plateau is underlain by the Karoo siliciclastics intruded by subhorizontal Karoo dolerite sills. Small hills (kopies), held up by the relatively resistant dolerite sills, locally rise above the plateau floor (King, 1951). One of the largest of these kopies is Hantam Mountain near Calvinia, which rises ~500 m above the plateau and is also underlain by flat-lying Karoo dolerites (Figure 2).

Quartz and pyroxene-bearing bedrock samples were collected at four locations along the great escarpment and from the interior plateau between Beaufort West and Calvinia. The geographical locations of the samples are marked in Figure 2; information on geographical coordinates, altitude and surface inclination is provided in Table 1.

Near Vanrhynspass, three TMG quartzite samples were collected from the edge of the escarpment (Table 1, Figure 3). Samples CA04/05 and 12 were collected from the flat, stable erosional surface close to the escarpment edge, whereas CA04/13 was collected from an inclined rim of the flat quartzite surface a few metres from the escarpment edge (Figure 3c). This latter sample was dated in order to assess the influence of lateral spalling of blocks on cosmogenic nuclide concentrations.

Karoo dolerite samples were collected from three different localities. From the summit of the escarpment near Beaufort West two samples were collected about 6 m apart at 1800 m elevation (Figure 4, Table 1). On the interior plateau four dolerite samples were collected at three different sites on top of Hantam Mountain near Calvinia, over a distance of ~2.5 km (Figures 2 and 5). CA04/02B is from the top of an isolated metre-sized block raised 70 cm above the surrounding flat erosional surface from which sample CA04/02A was collected (Figure 5c). This configuration was expected to reveal a difference in erosion between the upper and lower surfaces and to provide an opportunity to test the reliability of our dating methods.

Both the sampling sites near Beaufort West and on Hantam Mountain represent flat stable surfaces underlain by Karoo dolerites (Figures 4b and 5b). The last sample CA04/23A was collected from the top of a small dolerite hill (kopie, see Figure 6a) that rises a few tens of metres above the plateau floor in the vicinity of Williston (Figures 2 and 6).

Analytical procedure

The use of noble gas isotopes for surface exposure dating and determination of denudation rates involves some specific difficulties. Because they are stable, non-cosmogenic components always contribute to their total inventory as well. These components may have been trapped by the rock from the atmosphere or from crustal or mantle-derived fluids, or may have been produced within the rock by nuclear processes such as radioactive decay of U and Th, and it is crucial that they are successfully discriminated against those produced by cosmic-ray irradiation. For this purpose the following approaches have proven useful (*e.g.* Niedermann, 2002) and have been applied in this study:

1. Gas extraction is performed in several heating steps. This technique makes use of the different release characteristics of various components resulting in their partial separation.
2. An additional crushing extraction may reveal the isotopic composition of the components trapped in fluid inclusions or between grain boundaries. In contrast, the cosmogenic component is sited within the crystal lattice where it was produced.
3. For Ne, the data are plotted in three-isotope diagrams (Figure 7), where a two-component mixture of trapped and cosmogenic Ne plots along a characteristic mixing line (the so-called “spallation line”), whose slope corresponds to the $^{22}\text{Ne}/^{21}\text{Ne}$ production ratio (Niedermann, 2002). This ratio is different for quartz and pyroxene because it depends on the elements from which Ne is produced, *i.e.* Si only for quartz but Si and Mg for pyroxene. Data deviating from the spallation line in the three-isotope plot indicate the presence of a third component, such as nucleogenic ^{21}Ne and ^{22}Ne , which may be produced by nuclear reactions of alpha particles from U/Th decay with ^{18}O and ^{19}F , respectively.

In detail, the analytical procedure involved the following steps: After crushing and sieving the whole rock samples, the 250 to 500 μm fractions were used for further treatment. Pyroxene separates were prepared by etching the dolerite material in concentrated HCl, applying magnetic separation and density separation techniques, and final handpicking. Major element



Figure 3. (a) Great Escarpment at the Vanrhynspass with the position of the analysed samples. Fallen blocks of quartzite scattered along the escarpment slope can be seen. (b) Sample site CA04/05 on the edge of the escarpment at Vanrhynspass. (c) Sample site CA04/13 on the inclined rim of the stable erosional surface.

compositions were determined by X-ray fluorescence (XRF) analysis, using splits of ~400 mg of each separate.

For the preparation of clean quartz separates, a chemical treatment was applied, involving a first leach in HCl at a temperature of ~80°C for 4 hours, followed by a series of three leaches, each between 7 and 10 hours, in a diluted HF/HNO₃ mixture at 80 °C in an ultrasonic bath. The etching in the HF/HNO₃ mixture removed at least several microns of the surface of the quartz grains, thereby reducing the probability of contributions of nucleogenic ²¹Ne, which may be produced when alpha particles are injected from neighbouring U/Th-rich minerals and react with ¹⁸O in

the quartz (e.g. Niedermann, 2002). The details of the cleaning procedure have been described in Hetzel *et al.* (2002).

The noble gas analysis was carried out at GFZ Potsdam. The quartz samples were ground to <100 µm in an agate mill, while pyroxene samples were not treated further. Samples were then washed in acetone, dried by heating at ~90 °C overnight and wrapped in Al or Mo foil before being loaded into the sample carrousel above the extraction furnace. Samples were degassed by stepwise heating at 400, 600, 800, and 1200 °C for quartz; and at 600, 900 and 1750 °C for pyroxene. For all quartz and two of the pyroxene samples, crushing extractions were also performed on aliquots.

Table 2. Results of He and Ne analyses in pyroxene and quartz samples from the South African escarpment and interior plateau (see Table 1 and Figures 2-6 for details on sampling sites). Noble gas concentrations are in units of $\text{cm}^3 \text{STP/g}$, error limits are 2σ .

Sample	T	^4He	^{20}Ne	$^3\text{He}/^4\text{He}$	$^{22}\text{Ne}/^{20}\text{Ne}$	$^{21}\text{Ne}/^{20}\text{Ne}$
Weight	°C	10^{-8}	10^{-12}	10^{-6}	10^{-2}	10^{-2}
BW04/01 px	600	98.7	1740	2.395	10.137	0.2935
0.49994 g		±4.9	±100	±0.068	±0.072	±0.0047
	900	204	3.96	0.431	14.52	4.46
		±10	±0.59	±0.016	±0.77	±0.74
	1750	720	12.3	0.0180	16.44	13.7
		±52	±1.4	±0.0047	±0.57	±1.2
	Total	1023	1760	0.330	10.191	0.397
		±53	±100	±0.020	±0.072	±0.016
BW04/01B px	600	111.5	5.76	2.175	10.54	0.42
0.50075 g		±5.6	±0.79	±0.049	±0.72	±0.10
	900	304	6.60	0.215	14.21	3.79
		±22	±0.78	±0.014	±0.70	±0.38
	1750	64.1	34.1	0.185	11.81	1.67
		±3.2	±3.8	±0.020	±0.33	±0.14
	Total	480	46.5	0.667	11.99	1.82
		±23	±4.0	±0.031	±0.28	±0.12
0.66204 g	crushed	71.0	5.17	0.0254	10.27	0.319
		±4.3	±0.40	±0.0039	±0.28	±0.037
CA04/01 px	600	25.9	5810	6.25	10.142	0.2928
0.49951 g		±1.3	±340	±0.15	±0.066	±0.0041
	900	17.21	22.1	3.74	10.97	0.781
		±0.86	±1.5	±0.21	±0.32	±0.063
	1750	11.29	681	3.04	10.152	0.3607
		±0.56	±40	±0.19	±0.074	±0.0066
	Total	54.4	6510	4.79	10.146	0.3016
		±1.7	±340	±0.11	±0.059	±0.0038
CA04/02A px	600	16.33	1123	6.77	10.186	0.2943
0.50342 g		±0.82	±66	±0.25	±0.075	±0.0082
	900	15.70	14.2	2.56	11.29	0.888
		±0.78	±1.0	±0.13	±0.40	±0.056
	1750	10.81	384	1.220	10.258	0.3635
		±0.54	±23	±0.085	±0.079	±0.0078
	Total	42.8	1521	3.83	10.214	0.3173
		±1.3	±70	±0.13	±0.059	±0.0065
CA04/02B px	600	60.9	10.49	3.38	10.39	0.322
0.50134 g		±3.0	±0.95	±0.12	±0.50	±0.050
	900	38.8	93.0	1.976	10.68	0.523
		±1.9	±5.2	±0.074	±0.11	±0.023
	1750	8.60	953	4.52	10.199	0.3450
		±0.43	±52	±0.20	±0.067	±0.0048
	Total	108.3	1056	2.968	10.243	0.3604
		±3.6	±52	±0.077	±0.061	±0.0049
0.52760 g	crushed	9.44	292	0.123	10.194	0.299
		±0.57	±27	±0.057	±0.088	±0.010
CA04/03 px	600	36.3	7.10	5.53	10.40	0.328
0.50095 g		±2.2	±0.83	±0.17	±0.47	±0.060
	900	19.1	21.0	1.78	11.56	1.236
		±1.1	±1.6	±0.10	±0.25	±0.050
	1750	3.13	158	1.74	10.429	0.465
		±0.19	±10	±0.26	±0.062	±0.018
	Total	58.5	186	4.10	10.556	0.547
		±2.5	±10	±0.13	±0.063	±0.018

Table 2. continued

Sample	T	${}^4\text{He}$	${}^{20}\text{Ne}$	${}^3\text{He}/{}^4\text{He}$	${}^{22}\text{Ne}/{}^{20}\text{Ne}$	${}^{21}\text{Ne}/{}^{20}\text{Ne}$
Weight	${}^\circ\text{C}$	${}^{10^{-8}}$	${}^{10^{-12}}$	${}^{10^{-6}}$	${}^{10^{-2}}$	${}^{10^{-2}}$
CA 04/05 qz	400	0.643	13.01	0.038	10.974	1.177
1.31012 g		± 0.032	± 0.73	$+0.045/-0.038$	± 0.084	± 0.030
	600	13.26	46.5	0.0040	10.32	0.673
		± 0.66	± 2.4	$+0.0058/-0.0040$	± 0.22	± 0.022
	800	25.6	60.3	0.0004	10.26	0.349
		± 1.3	± 3.2	$+0.0016/-0.0004$	± 0.10	± 0.012
	1200	4.99	2.47	0.0025	10.56	1.48
		± 0.25	± 0.45	$+0.0073/-0.0025$	± 0.22	± 0.29
	Total	44.5	122.3	0.0023	10.365	0.583
		± 1.5	± 4.1	± 0.0022	± 0.098	± 0.015
1.00551 g	crushed	0.894	60.3	0.16	10.305	0.320
		± 0.046	± 3.1	± 0.12	± 0.087	± 0.011
CA 04/12 qz	400	5.63	150.8	0.007	10.679	0.718
0.70418 g		± 0.28	± 7.8	$+0.015/-0.007$	± 0.064	± 0.011
	600	13.86	91.6	0.003	10.317	0.362
		± 0.69	± 4.8	$+0.014/-0.003$	± 0.080	± 0.014
	800	24.2	48.9	0.0013	10.34	0.346
		± 1.2	± 2.8	$+0.0059/-0.0013$	± 0.12	± 0.018
	1200	17.67	3.36	0.0008	10.44	0.89
		± 0.88	± 0.91	$+0.0068/-0.0008$	± 0.27	± 0.17
	Total	61.4	294.5	0.0021	10.507	0.548
		± 1.7	± 9.6	$+0.0046/-0.0021$	± 0.046	± 0.010
1.00375 g	crushed	0.1100	72.7	0.90	10.240	0.316
		± 0.0089	± 5.4	± 0.77	± 0.072	± 0.011
CA 04/13 qz	400	9.72	141.3	0.0089	10.485	0.607
0.70090 g		± 0.58	± 8.8	± 0.0070	± 0.048	± 0.014
	600	16.7	69.6	0.0030	10.276	0.349
		± 1.0	± 4.4	$+0.0087/-0.0030$	± 0.058	± 0.014
	800	23.3	52.4	<0.010	10.346	0.3554
		± 1.4	± 3.5		± 0.091	± 0.0085
	1200	11.04	2.33	0.0001	10.47	1.33
		± 0.66	± 0.93	$+0.0074/-0.0001$	± 0.55	± 0.40
	Total	60.8	266	0.0023	10.403	0.496
		± 1.9	± 10	$+0.0048/-0.0023$	± 0.035	± 0.011
1.00294 g	crushed	0.397	104.2	0.47	10.256	0.3156
		± 0.032	± 7.7	± 0.22	± 0.036	± 0.0074
CA04/23A px	600	25.8	1126	8.25	10.299	0.2956
0.50706 g		± 1.3	± 66	± 0.25	± 0.078	± 0.0090
	900	29.1	33.1	1.698	10.84	0.908
		± 1.5	± 2.1	± 0.093	± 0.17	± 0.045
	1750	15.94	797	1.086	10.215	0.3496
		± 0.80	± 47	± 0.081	± 0.068	± 0.0069
	Total	70.8	1956	3.95	10.274	0.3280
		± 2.1	± 81	± 0.14	± 0.053	± 0.0061

The noble gases were analysed in a VG5400 mass spectrometer according to procedures described in Niedermann *et al.* (1997).

Results

The complete results of He and Ne analyses are presented in Table 2. The cosmogenic ${}^3\text{He}$ concentrations in the pyroxene separates (Table 3) have been calculated assuming a ${}^3\text{He}/{}^4\text{He}$ ratio of the non-

cosmogenic (*i.e.*, trapped and radiogenic) component of $(0.028 \pm 0.028) \times 10^{-6}$, as derived from the crushing extractions of two samples (Table 2) and by taking into account the possible presence of additional radiogenic ${}^4\text{He}$ produced in situ by U/Th decay in these 183 Ma (${}^{40}\text{Ar}/{}^{39}\text{Ar}$ age, Duncan *et al.*, 1997) old minerals (the latter component does not show up in a crushing extraction). In quartz, cosmogenic ${}^3\text{He}$ is not quantitatively retained (*e.g.* Niedermann, 2002), as also

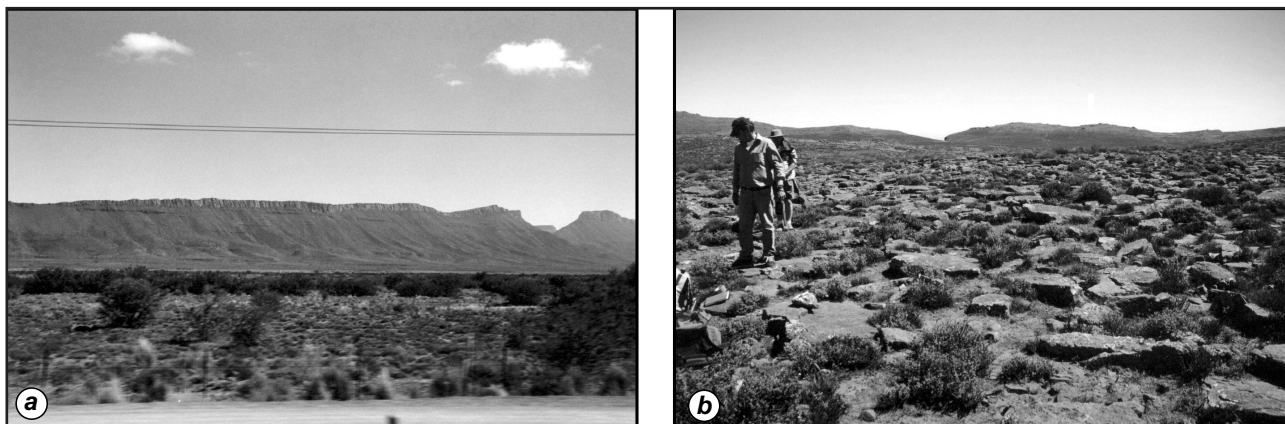


Figure 4. (a) Great Escarpment near Beaufort West. (b) Sample site BW04/01 on the top of the escarpment near Beaufort West.

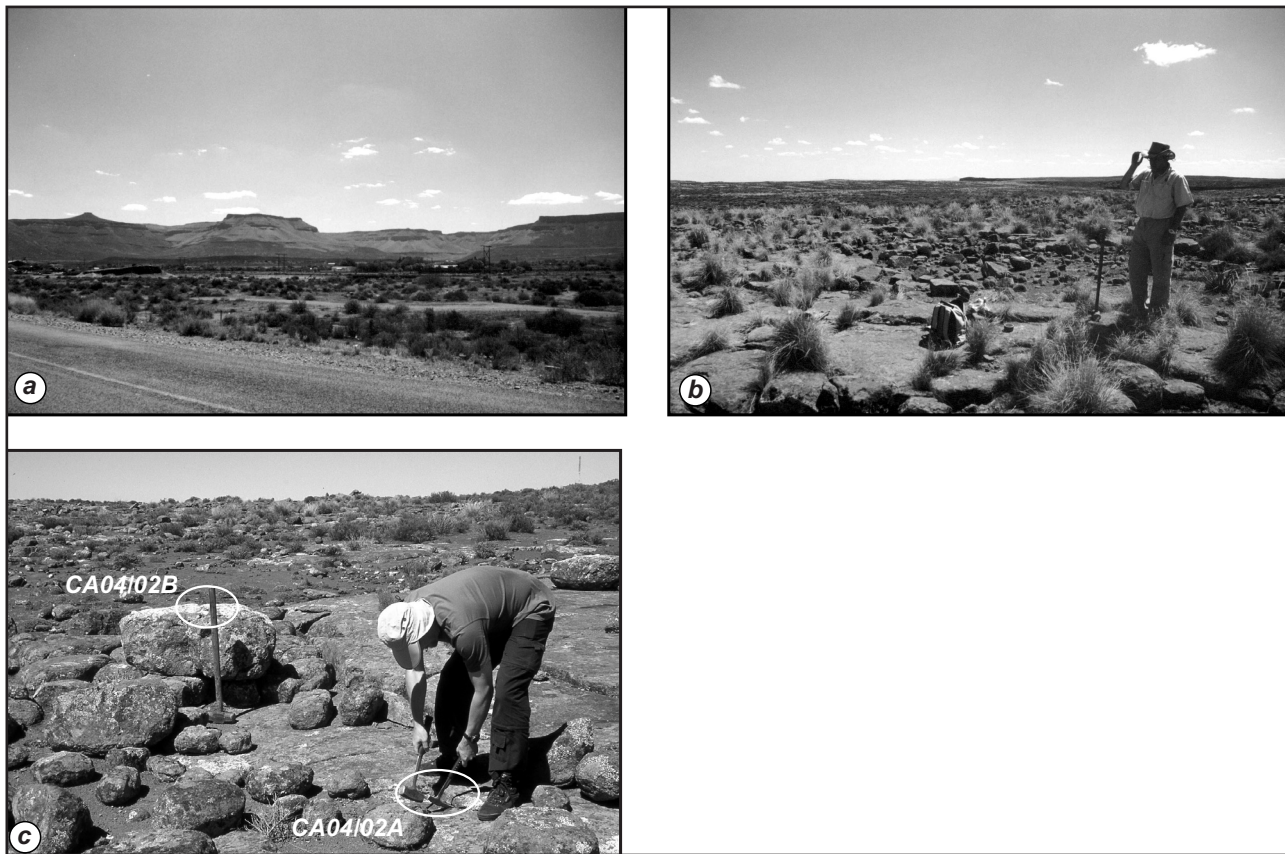


Figure 5. (a) Hantam Mountain near Calvinia. (b) Sample site CA04/03 on the top of Hantam Mountain. (c) Dolerite-capped erosional surface on the top of Hantam Mountain near Calvinia with the location of samples CA04/02A and B.

evident from the extremely low $^3\text{He}/^4\text{He}$ ratios (Table 2); therefore we do not report cosmogenic ^3He concentrations for the quartz samples.

To determine the cosmogenic ^{21}Ne concentrations, the stepwise heating data were first plotted in three-isotope diagrams (Figure 7). For the pyroxene samples, all data points (except for the 1750 °C step of BW04/01) lie on or very close to the spallation line (Schäfer *et al.*, 1999), indicating that contributions of nucleogenic ^{21}Ne produced by $^{18}\text{O}(\alpha, n)^{21}\text{Ne}$ are negligible. For BW04/01, a correction for nucleogenic Ne was applied according to the assumption that the $^{22}\text{Ne}/^{20}\text{Ne}$ ratio is indicative for the cosmogenic component (*i.e.*, no nucleogenic

^{22}Ne is present; cf. Niedermann, 2002). Since the correction amounts to more than 50%, the result for this sample may be less reliable than for the other pyroxene separates. Trapped Ne was assumed to be atmospheric in the pyroxenes as both crushing extractions yielded isotopic compositions consistent with that of air Ne within error limits (Table 2).

For quartz, the trapped Ne is slightly enriched in ^{21}Ne compared to atmospheric abundances and agrees for the three samples (Table 2 and Figure 7); therefore cosmogenic ^{21}Ne excesses were calculated relative to a weighted mean $^{21}\text{Ne}/^{20}\text{Ne}$ ratio of 0.003167 ± 0.000054 . The majority of the stepwise heating data is consistent

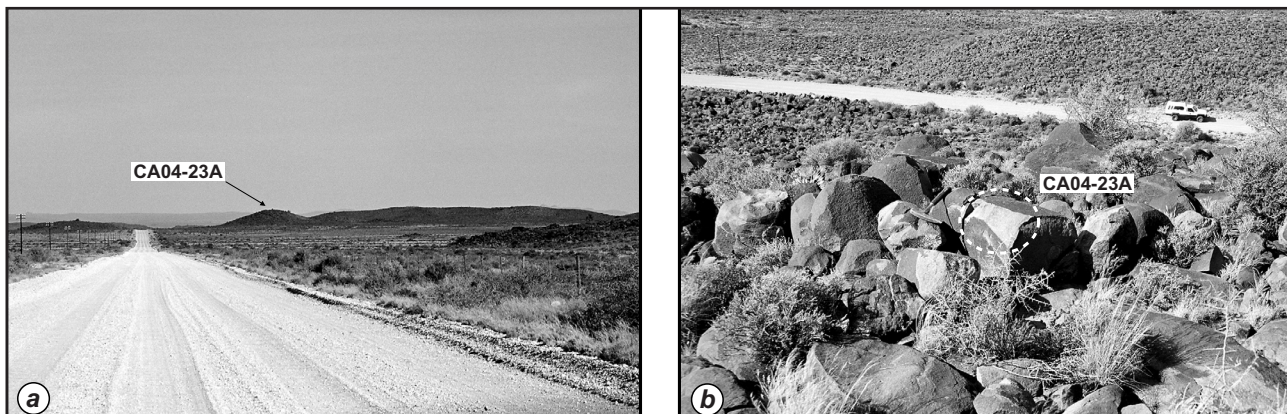


Figure 6. (a) Small dolerite hill (kopie) rising a few tens of metres above the plateau near Williston. (b) Sample site CA04/23A on the top of the hill.

with the spallation line for quartz (Niedermann *et al.*, 1993), except for all 1200°C data and for the 400 and 600°C steps of CA04/05. In the 1200°C steps, a contribution of nucleogenic Ne, most probably produced in mineral or fluid inclusions, is quite typical for many quartz samples. Since cosmogenic Ne is quantitatively released from quartz below 800°C (Niedermann, 2002) and the ≤800°C data do not show significant deviations from the spallation line for CA04/12 and 13, the accuracy of the cosmogenic ^{21}Ne concentration is not affected by the 1200°C data, which contribute less than 5% to the total ^{21}Ne excess. For CA04/05, the position of the 400 and 600°C data below the spallation line may just indicate isotopic mass fractionation, which is also not unusual for quartz (*e.g.* Hetzel *et al.*, 2002). Cosmogenic ^{21}Ne has therefore been calculated by summing up the ^{21}Ne excesses in the 400 to 800°C steps for all quartz samples.

The resulting concentrations of cosmogenic ^3He (pyroxenes only) and ^{21}Ne are given in Table 3. In order to convert these into model exposure ages or erosion rates, the production rates for the particular mineral

chemistry and sample locations have to be known. For quartz we have used a ^{21}Ne production rate of 19 atoms $\text{g}^{-1} \text{a}^{-1}$ at sea level and high latitude (Niedermann, 2000), which was scaled to the sampling locations using the procedure of Dunai (2000). We used geographical rather than geomagnetic latitude for scaling, which is expected to average out variations of the geomagnetic pole position over a few hundred to a few thousand years (*e.g.* Sternberg, 1996). We did not apply any corrections for variations of the geomagnetic field intensity in the past, however. Such variations may have increased time-integrated production rates over a few hundred thousand years compared to the present ones by up to 15% at ~30°S (Dunai, 2001), but possibly much less (Masarik *et al.*, 2001). Corrections for exposure geometry (surface inclination and shading) are negligible (<1%) except for CA04/13 (2.3%). The geometry of boulders (Masarik and Wieler, 2003) was not taken into account because it is impossible to assess how it may have changed during the exposure. In any case such corrections would be <10%, and since they are opposite to those caused by geomagnetic field

Table 3. Concentrations of cosmogenic ^3He and ^{21}Ne in the investigated pyroxene and quartz separates, as well as adopted ^3He and ^{21}Ne production rate values (P_3 and P_{21} ; in units of atoms $\text{g}^{-1} \text{a}^{-1}$). For pyroxenes, these production rates were calculated according to different methods which disagree considerably (see text); for quartz they are based on Niedermann (2000). In both cases the values for sea level and high latitude were scaled to the sampling location (Table 1) using Dunai (2000) with no further correction except for CA04/13, where a 2.3% correction takes into account the 30° surface inclination.

Sample	$^3\text{He}_c$	$^{21}\text{Ne}_c$	P_3	P_{21}	P_3	P_{21}
	10^6 atoms/g		<i>Masarik and Reedy (1996)</i>	<i>(1996)</i>	<i>Kober et al. (2005)</i>	
BW04/01	84.9+5.6/-4.3	23.7+2.0/-1.7	333	76.0	440	103.5
BW04/01B	82.3 ± 4.6	19.0 ± 1.0	327	73.9	452	98.9
CA04/01	69.6 ± 2.8	$14.7+2.2/-1.5$	264	61.8	359	83.6
CA04/02A	43.7 ± 2.0	$9.3+2.2/-0.9$	260	59.0	344	80.2
CA04/02B	85.5 ± 3.7	18.3 ± 1.6	256	58.0	356	77.6
CA04/03	64.0 ± 3.8	12.52 ± 0.95	256	55.1	343	74.5
CA04/05	–	7.98 ± 0.46	–	27.0^1	–	–
CA04/12	–	17.7 ± 1.0	–	27.2^1	–	–
CA04/13	–	12.17 ± 0.91	–	26.5^1	–	–
CA04/23A	74.6 ± 3.6	$17.0+3.1/-1.7$	204	50.5	283	67.8

¹ Based on Niedermann (2000)

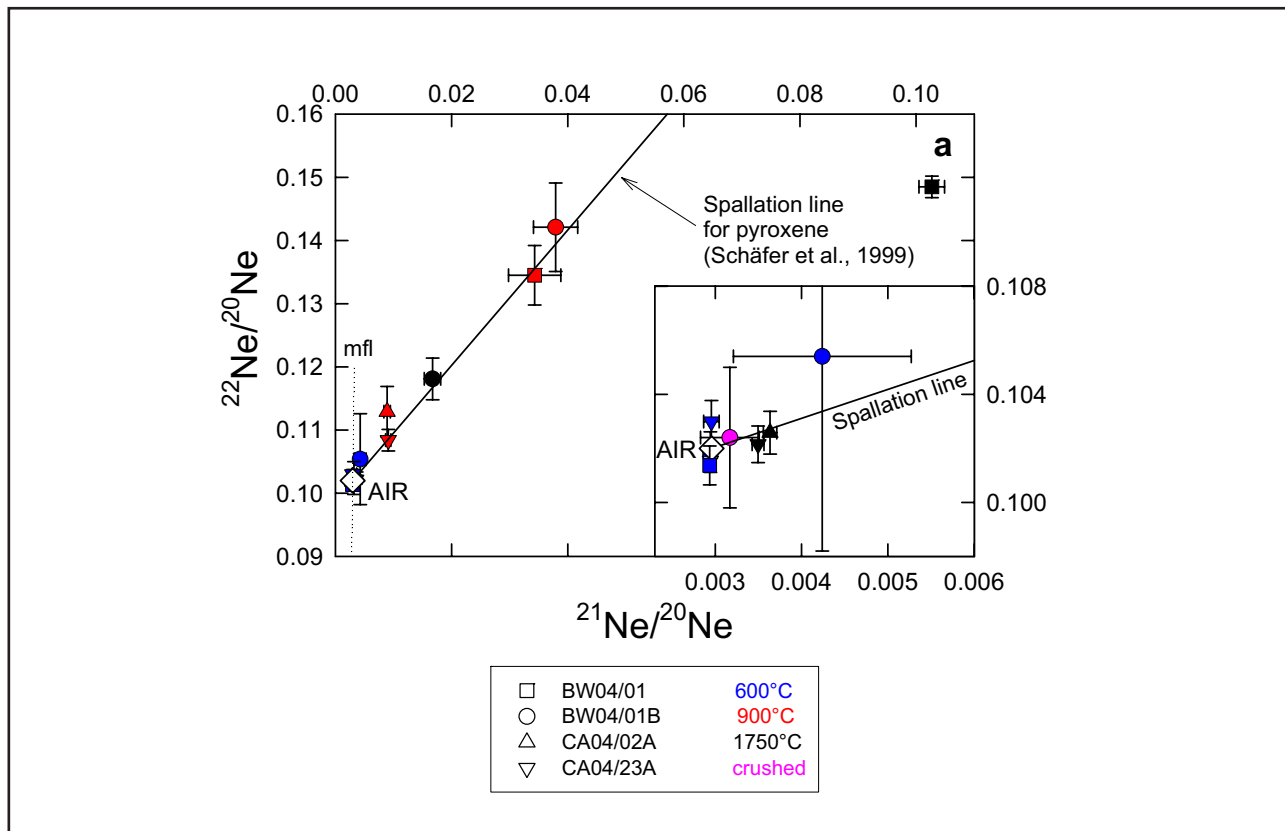


Figure 7. Ne three-isotope plots showing the isotopic compositions of stepwise heating data for pyroxene (**a**) and quartz samples (**b**). The spallation lines for pyroxene and quartz, respectively, are the mixing lines between atmospheric Ne and cosmogenic Ne in those minerals; mfl denotes the mass fractionation line. Note different scales in (a) and (b). The data plotting close to air are shown enlarged in the insets. Various symbols show different samples, colours denote individual heating steps and crushing extractions (see legends). Three pyroxene samples are not shown here for clarity; their data plot along the spallation line as well. Unlike the data given in Table 2, those plotted here (except for crushing extractions) have not been corrected for analytical blanks because this correction only increases relative excesses and uncertainties without changing the general picture.

intensity variations the net error introduced by neglecting both effects will be small.

For pyroxene, there are several methods available to calculate ${}^3\text{He}$ and ${}^{21}\text{Ne}$ production rates based on their major element composition; in case of ${}^3\text{He}$ it is also possible to use a chemistry-independent value of ~ 115 atoms $\text{g}^{-1} \text{a}^{-1}$ at sea level and high latitude, which is based on various experimental determinations (e.g. Cerling and Craig, 1994; Licciardi *et al.*, 1999; Dunai and Wijbrans, 2000). Niedermann *et al.* (2007) have recently pointed out that these different methods can be grouped in two sets. Consistent ${}^3\text{He}$ and ${}^{21}\text{Ne}$ exposure ages are obtained for each set of methods, while there is a discrepancy of up to 40% when changing from one set of methods to the other one. Since Niedermann *et al.* (2007) have not been able to assess which methods yield the more reliable production rates, we present two values each for the ${}^3\text{He}$ and ${}^{21}\text{Ne}$ production rates in the pyroxene samples (Table 3). They were calculated according to the methods of Masarik and Reedy (1996) and Kober *et al.* (2005), respectively, which are representative for either of the two sets (Niedermann *et al.*, 2007). The major element compositions used for these calculations are given in Table 4.

${}^3\text{He}$ (pyroxene only) and ${}^{21}\text{Ne}$ exposure ages were calculated from the concentrations and production rates given in Table 3 and are shown in Table 5. They are in fact minimum exposure ages because the underlying assumption of no erosion is clearly not correct; nevertheless they give an impression of the prevailing timescales for landscape modification. For the pyroxenes, the He and Ne ages calculated based on the same production rate method agree in most cases within error limits, with the exception of BW04/01 (Table 5). It is possible that this pyroxene separate, which showed a substantial contribution of nucleogenic ${}^{21}\text{Ne}$ in the 1750°C step (Figure 7a) and the highest concentration of ${}^4\text{He}$, was less pure than the other ones and contained an admixture of minerals rich in U and Th and not as retentive for cosmogenic He as pyroxene. In this case the Ne data could be more reliable than the He data. On the other hand, we may have underestimated the correction for nucleogenic ${}^{21}\text{Ne}$ if some nucleogenic ${}^{22}\text{Ne}$ was also present in the sample. BW04/01 is also the only sample for which we could derive an ${}^{38}\text{Ar}$ exposure age with an accuracy better than 50%. Its cosmogenic ${}^{38}\text{Ar}$ concentration of $(17.5 \pm 5.0) \times 10^6$ atoms/g corresponds to a minimum exposure age

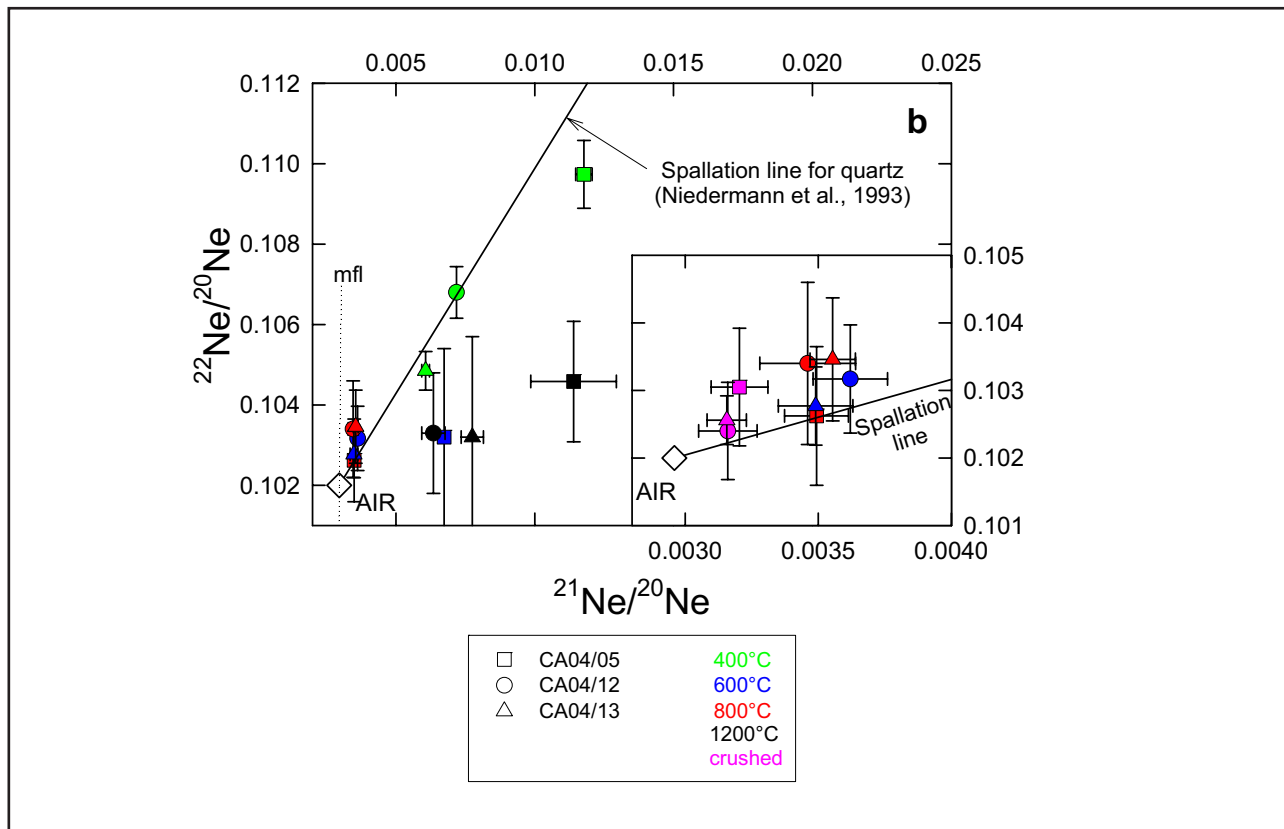


Figure 7. continued

of 280 ± 81 ka or 210 ± 61 ka, depending on whether the low or the high value for the ^{38}Ar production rate (as related to the two sets of He and Ne production rates mentioned above) given by Niedermann *et al.* (2007) is used. These ages agree with both the He and Ne ages within uncertainties.

Finally, we have calculated maximum erosion rates (assuming infinite exposure) for the sampled surfaces (Table 5), assuming a cosmic ray attenuation length of 167 g/cm² (Masarik and Reedy, 1995) and a rock density of 2.7 g/cm³ for the quartzites and 3.0 g/cm³ for the dolerites. In the case of sample CA04/13 the result was corrected for the increased attenuation length beneath inclined surfaces according to Hermanns *et al.* (2004).

Discussion

The estimated minimum exposure ages at the edge of the escarpment near Vanrhynspass are between 0.30 and 0.65 Ma, and the corresponding maximum denudation rates vary between 1 and 2 m/Ma. The correlation between the obtained ages and the samples' altitudes (Tables 1 and 5) confirms the expectation that the highest surface is also the oldest one (thus the least eroded). The old age of sample CA04/13 (0.50 Ma) suggests that this site represents a remnant of the stable horizontal surface rather than the steep face of the escarpment's cliff (Figure 3).

Our analyses of dolerite samples provide reliable estimates for the vertical denudation rates in both the escarpment area and the interior plateau. Summarising

the results from Table 5, we can report mean vertical denudation rates between ~1.5 and 3 m/Ma from these sites, not including the highest value from the lower level at the CA04/02 site. The ^3He and ^{21}Ne denudation rates derived from the summit of Hantam Mountain and the top of the escarpment near Beaufort West are remarkably similar. The results show analogous rates for similar lithologies exposed at similar landform sites. At Vanrhynspass, on the other hand, denudation rates are lower than those obtained for the Hantam Mountain and Beaufort West sites (Table 5), suggesting a slower denudation rate of the quartzite-dominated surfaces compared to the dolerites. The ~800 m high flat land surface preserved between the Vanrhynspass escarpment and the inland limit of the dolerite sills could then be considered as a remnant of an interfluvial domain between the Krom and Doring rivers, which is now being slowly removed through headward erosion (Figure 2). The present escarpment position reflects the differential resistance to erosion of the exposed rocks in this area (Figure 2; and King, 1951). Along the coast, a low lying (from 0 to 200 m above sea level), up to 80 km wide flat plain is developed in soft, fine-grained clastic sedimentary rocks of Neoproterozoic age, flanked on the inland side by the escarpment itself and its elevated plateau that is underlain by TMG quartzites. Farther inland the plateau gradually rises to ~1000 m elevation, where the quartzites are overlain by the Karoo shales and sandstones intruded by the relatively resistant flat-lying dolerite sills.

Table 4. Concentrations of major elements (wt. %) in the investigated pyroxene separates as determined by XRF analysis and used for calculation of ^3He and ^{21}Ne production rates.

Sample	O	Na	Mg	Al	Si	Ca	Ti	Fe
BW04/01	43.2	0.09	10.77	0.95	24.7	10.89	0.22	8.63
BW04/01B	42.3	<0.07	10.77	0.58	24.3	5.17	0.24	16.28
CA04/01	43.0	0.05	11.51	0.74	24.6	7.24	0.22	12.41
CA04/02A	42.9	0.09	10.74	0.85	24.5	10.10	0.23	9.84
CA04/02B	42.5	0.04	10.83	0.53	24.5	4.60	0.23	16.84
CA04/03	42.3	0.10	9.57	0.69	24.3	9.51	0.29	12.62
CA04/23A	42.5	0.11	12.50	0.90	24.1	4.42	0.18	13.91

The influence of the present climatic conditions on the denudation rates is suggested by the fact that the lowest value among dolerite lithologies of 1.5 to 2.2 m/Ma was obtained from the sample near Williston, situated 250 km inland from the west coast, where the mean annual precipitation is less than 100 mm (Figure 2). These climatic conditions have persisted at least for the last 10 to 12 Ma in western and central South Africa because they are directly controlled by the cold Benguela current that runs parallel to the southwest African coast (e.g. Ségalen *et al.*, 2006 and references therein). Although the timing of the onset of the Benguela current is part of a still ongoing debate (Ségalen *et al.*, 2006), its origin is almost certainly related to the opening of the Drake passage, the southern ocean's main gateway, at about 50 Ma (e.g. Livermore *et al.*, 2005; Scher and Martin, 2006). Some authors propose, therefore, that similar climatic conditions have

persisted across southern Africa throughout much of the Cenozoic, and that the denudation rates estimated from cosmogenic nuclide analyses might be extrapolated over the whole of the Cenozoic (e.g. Cockburn *et al.*, 2000). This hypothesis is now questioned by the recent recognition of at least two periods of enhanced rainfall and drainage reactivation in the past 20 Ma (Bamford, 2000; Tyson and Partridge, 2000; Brandt *et al.*, 2005).

On the other hand, denudation rates during the Cretaceous, as inferred from apatite fission track analyses, were greater than in the Cenozoic by an order of magnitude, with discrete episodes of accelerated denudation higher still by another order of magnitude in the mid-Cretaceous (Tinker, 2005; de Wit, 2007; Tinker *et al.*, in review; Kounov *et al.*, in review). Up to 2 km of sediments were removed during the Cretaceous from the same high plateau sites sampled for this study.

Table 5. Minimum exposure ages T_3 and T_{21} (ka) and maximum erosion rates ε_3 and ε_{21} (m/Ma) of the sampled surfaces. For pyroxenes, data are again reported according to both the production rate calculation methods of (a) Masarik and Reedy (1996) and (b) Kober *et al.* (2005), respectively. Error limits (2σ) reflect only the analytical uncertainty of the noble gas analysis.

Sample	T_3 a	T_{21} a	T_3 b	T_{21} b	ε_3 a	ε_{21} a	ε_3 b	ε_{21} b
BW04/01	255 +17/-13	312 +26/-22	193 +13/-10	229 +19/-16	2.18 +0.11/-0.14	1.79 +0.13/-0.15	2.88 +0.15/-0.19	2.43 +0.17/-0.21
BW04/01B	252 ±14	257 ±14	182 ±10	192 ±10	2.21 ±0.12	2.17 ±0.11	3.06 ±0.17	2.90 ±0.15
CA04/01	264 ±11	238 +36/-24	194 ±8	176 +26/-18	2.11 ±0.08	2.34/ +0.24/-0.35	2.87 ±0.12	3.17 +0.32/-0.47
CA04/02A	168 ±8	157 +37/-16	127 ±6	115 +27/-11	3.31 ±0.15	3.55 +0.35/-0.84	4.38 ±0.20	4.82 +0.47/-1.15
CA04/02B	334 ±14	316 ±28	240 ±10	236 ±21	1.67 ±0.07	1.76 ±0.15	2.32 ±0.10	2.36 ±0.21
CA04/03	250 ±15	227 ±17	187 ±11	168 ±13	2.23 ±0.13	2.45 ±0.19	2.98 ±0.18	3.31 ±0.25
CA04/05	—	296 ±17	— —	— —	— —	2.09 ±0.12	— —	— —
CA04/12	—	651 ±37	— —	— —	— —	0.95 ±0.05	— —	— —
CA04/13	—	495 ±17	— —	— —	— —	1.14 ¹ ±0.09	— —	— —
CA04/23A	366 ±18	337 +61/-34	264 ±13	251 +46/-25	1.52 ±0.07	1.65 +0.17/-0.30	2.11 ±0.10	2.22 +0.22/-0.40

¹Erosion rate corrected for surface inclination according to Hermanns *et al.* (2004).

These results are consistent with significant changes in the climate, but also with important tectonic regime changes since the Cretaceous, because the Cretaceous was a time of significant active, regional uplift (Raab *et al.*, 2002; Doucouré and de Wit, 2003; Tinker, 2005; de Wit, this volume; Tinker *et al.*, in review; Kounov *et al.*, in review). Lower denudation rates today and throughout the Cenozoic are, therefore, also a consequence of the adjustment to the base level established during this Cretaceous uplift phase.

The importance of the climate conditions is also reflected by the differences in the denudation rates reported for the Drakensberg escarpment area (Fleming *et al.*, 1999) and the areas explored by the present study (Figure 1). The Indian Ocean coast is characterised by a hot and humid climate, significantly different from the climate typical for the western coastal regions of South Africa. It must be mentioned that the relations between the climate and the denudation rates are not always straightforward and the high denudation rates in the Drakensberg escarpment (up to 6 m/Ma, Fleming *et al.*, 1999) are only possible due to the absence of significantly developed vegetation and soil on its summit, which would hamper the erosion.

Nonetheless, these large climatic variations may also mask more subtle local variations in weathering conditions as reflected, for example, in the results for two samples from Hantam Mountain. Sample CA04/02A from the flat erosional surface yields a higher denudation rate by a factor of 2 compared to that of CA04/02B from the upper surface of the higher exposed block (Figure 5c, Table 5). This interesting result suggests that even a minimum of running/standing water on the lower, flat surface, will enhance the weathering and erosion caused by the combined action of frost and slaking, which are the dominant erosional agents affecting this area. This observation provides important information about the erosional mechanism active on the flat summits and stresses the importance of further analyses for better understanding the dynamics of the local, small-scale landscape sculpturing in southern Africa.

Conclusions

Cosmogenic nuclide analyses are an excellent and rather unique tool to investigate the influence of lithology, climate and tectonics on landscape evolution, one of the most important goals of geomorphology investigations today. The data reported in this paper provide new insights into the erosion processes that have shaped southern Africa:

1. Denudation rates at the summit of the great escarpment and inland plateau for at least the last few hundred thousand years are more than an order of magnitude lower than those in the Cretaceous as estimated from apatite fission track analysis.
2. Our results suggest that local variations in climate and lithology both control the resulting patterns of the present denudation across different landform

sites on the high plateau and along its flanking escarpment.

Acknowledgements

We thank Peter Pilz for help with the mineral separation, Rudolf Naumann for performing the XRF analyses, and Enzio Schnabel for running the noble gas mass spectrometers. Constructive reviews by Kerry Gallagher and Joerg Schaefer have helped to improve the quality of the paper. This work was supported by Inkaba yeAfrica funds, in South Africa by DST, NRF and The Claude Leon Foundation postdoctoral fellowship (to Alexandre Kounov), and in Germany by the GeoForschungsZentrum Potsdam. This is AEON contribution 38, and Inkaba yeAfrica contribution number 23.

References

- Bamford, M. (2000). Cenozoic macro-plants. In: T.C. Partridge and R.R. Maud (Editors), *The Cenozoic of Southern Africa*, Oxford University Press, 351-356.
- Beaumont, C., Kooi, H., and Willet, S.D. (2000). Coupled tectonic-surface process models with applications to rifted margins and collisional orogens. In: M.A. Summerfield (Editor), *Geomorphology and Global Tectonics*, John Wiley and Son, New York, United States of America, 29-55.
- Bierman, P.R. and Caffee, M. (2001). Slow rates of rock surface erosion and sediment production across the Namib desert and escarpment, Southern Africa. *American Journal of Science*, **301**, 326-358.
- Bierman, P.R. and Nichols, K.K. (2004). Rock to sediment, slope to sea with ¹⁰Be-rates of landscape change. *Annual Review of Earth and Planetary Sciences*, **32**, 215-255.
- Brandt, D., Andreoli, M. and McCarthy, T.S. (2005). The Late Mesozoic paleosoils and Cenozoic fluvial deposits at Vaalputs, Namaqualand, South Africa. Possible depositional mechanism and their bearing on the evolution of the continental margin. *South African Journal of Geology*, **108**, 267-280.
- Brown, R.W., Gallagher, K., Gleadow, A.J.W. and Summerfield, M.A. (2000). Morphotectonic evolution of the South Atlantic margins of Africa and South America. In: M.A. Summerfield (Editor), *Geomorphology and Global Tectonics*, John Wiley & Son, New York, United States of America, 255-284.
- Brown, R.W., Summerfield, M.A. and Gleadow, A.J.W. (2002). Denudation history along a transect across the Drakensberg Escarpment of southern Africa derived from apatite fission track thermochronology. *Journal of Geophysical Research*, **107**, 2350, doi:10.1029/2001JB000745.
- Cerling, T.E. and Craig, H. (1994). Cosmogenic ³He production rates from 39°N to 46°N latitude, western United States of America and France. *Geochimica et Cosmochimica Acta*, **58**, 249-255.
- Cockburn, H.A.P., Brown, R.W., Summerfield, M.A. and Seidl, M.A. (2000). Quantifying passive margin denudation and landscape development using a combined fission-track thermochronometry and cosmogenic isotope analysis approach. *Earth and Planetary Science Letters*, **179**, 429-435.
- de Wit, M.J. The Kalahari Epeirogeny and climate change: differentiating cause and effect from core to space. *South African Journal of Geology*, **110**, 367-392.
- Doucouré, C.A. and de Wit, M.J. (2003). Old inherited origin for the present near bimodal topography of Africa. *Journal of African Earth Sciences*, **36**, 371-388.
- Dunai, T.J. (2000). Scaling factors for production rates of in situ produced cosmogenic nuclides: a critical re-evaluation. *Earth and Planetary Science Letters*, **176**, 157-169.
- Dunai, T.J. (2001). Influence of secular variation of the geomagnetic field on production rates of in situ produced cosmogenic nuclides. *Earth and Planetary Science Letters*, **193**, 197-212.
- Dunai, T.J. and Wijbrans, J.R. (2000). Long-term cosmogenic ³He production rates (152 ka – 1.35 Ma) from ⁴⁰Ar/³⁹Ar dated basalt flows at 29°N latitude. *Earth and Planetary Science Letters*, **176**, 147-156.
- Duncan, R.A., Hooper, P.R., Rehacek, J., Marsh, J.S. and Duncan, A.R. (1997). The timing and duration of the Karoo igneous event, southern Gondwana.

- Journal of Geophysical Research*, **102**, 18127-18138.
- Fleming, A., Summerfield, M.A., Stone, J.O.H., Fifield, L.K. and Cresswell, R.G. (1999). Denudation rates for the southern Drakensberg escarpment, SE Africa, derived from in-situ-produced cosmogenic ^{36}Cl : initial results. *Journal of the Geological Society, London*, **156**, 209-212.
- Hermanns, R.L., Niedermann, S., Ivy-Ochs, S. and Kubik, P.W. (2004). Rock avalanching into a landslide-dammed lake causing multiple dam failure in Las Conchas valley (NW Argentina) – evidence from surface exposure dating and stratigraphic analyses. *Landslides*, **1**, 113-122.
- Hetzel, R., Niedermann, S., Ivy-Ochs, S., Kubik, P.W., Tao, M. and Gao, B. (2002). ^{21}Ne versus ^{10}Be and ^{26}Al exposure ages of fluvial terraces: the influence of crustal Ne in quartz. *Earth and Planetary Science Letters*, **201**, 575-591.
- King, L.C. (1951). South African Scenery, *Oliver and Boyd, London, United Kingdom*, 379pp.
- King, L.C. (1967). The Morphology of the Earth. *Oliver and Boyd, Edinburgh, United Kingdom*, 699 pp.
- Kober, F., Ivy-Ochs, S., Leya, I., Baur, H., Magna, T., Wieler, R. and Kubik, P.W. (2005). In situ cosmogenic ^{10}Be and ^{21}Ne in sanidine and in situ cosmogenic ^3He in Fe-Ti-oxide minerals, *Earth and Planetary Science Letters*, **236**, 404-418.
- Kounov, A., Viola, G., de Wit, M.J. and Andreoli, M. (in review). Tectonic evolution and denudation of the Atlantic passive margin: New insights from apatite fission-track analysis on the Western coast of South Africa. In: F. Lisker, B. Ventura, and U. Glasmacher, (Editors), Thermochronological methods: from paleotemperature constraints to landscape evolution models. *Geological Society, London, Special Publications*.
- Licciardi, J.M., Kurz, M.D., Clark, P.U. and Brook, E.J. (1999). Calibration of cosmogenic ^3He production rates from Holocene lava flows in Oregon, USA, and effects of the Earth's magnetic field. *Earth and Planetary Science Letters*, **172**, 261-271.
- Livermore, R., Nankivell, A., Eagles, G., and Morris, P. (2005). Paleogene opening of Drake Passage. *Earth and Planetary Science Letters*, **236**, 459-470.
- Masarik, J. and Reedy, R.C. (1995). Terrestrial cosmogenic-nuclide production systematics calculated from numerical simulations. *Earth and Planetary Science Letters*, **136**, 381-395.
- Masarik, J. and Reedy, R.C. (1996). Monte Carlo simulation of in-situ-produced cosmogenic nuclides. *Radiocarbon*, **38**, 163.
- Masarik, J. and Wieler, R. (2003). Production rates of cosmogenic nuclides in boulders. *Earth and Planetary Science Letters*, **216**, 201-208.
- Masarik, J., Frank, M., Schäfer, J.M. and Wieler, R. (2001). Correction of in situ cosmogenic nuclide production rates for geomagnetic field intensity variations during the past 800,000 years. *Geochimica et Cosmochimica Acta*, **65**, 2995-3003.
- Niedermann, S. (2000). The ^{21}Ne production rate in quartz revisited. *Earth and Planetary Science Letters*, **183**, 361-364.
- Niedermann, S. (2002). Cosmic-ray produced noble gases in terrestrial rocks: Dating tools for surface processes. In: D. Porcelli, C. Ballantine, R. Wieler, (Editors), *Noble Gases in Geochemistry and Cosmochemistry, Reviews in Mineralogy and Geochemistry*, **47**, 731-784.
- Niedermann, S., Graf, T. and Marti, K. (1993). Mass spectrometric identification of cosmic-ray-produced neon in terrestrial rocks with multiple neon components. *Earth and Planetary Science Letters*, **118**, 65-73.
- Niedermann, S., Bach, W. and Erzinger, J. (1997). Noble gas evidence for a lower mantle component in MORBs from the southern East Pacific Rise: Decoupling of helium and neon isotope systematics. *Geochimica et Cosmochimica Acta*, **61**, 2697-2715.
- Niedermann, S., Schaefer, J.M., Wieler, R. and Naumann, R. (2007). The production rate of cosmogenic ^{38}Ar from calcium in terrestrial pyroxene. *Earth and Planetary Science Letters*, **257**, 596-608.
- Raab, M.J., Brown, R.W., Gallagher, K., Carter, A. and Weber, K. (2002). Late Cretaceous reactivation of major crustal shear zones in northern Namibia: constraints from apatite fission track analysis. *Tectonophysics*, **349**, 75-92.
- Schäfer, J.M., Ivy-Ochs, S., Wieler, R., Leya, I., Baur, H., Denton, G.H. and Schlüchter, C. (1999). Cosmogenic noble gas studies in the oldest landscape on earth: surface exposure ages of the Dry Valleys, Antarctica. *Earth and Planetary Science Letters*, **167**, 215-226.
- Scher, H.D. and Martin, E.E. (2006). Timing and climatic consequences of the opening of the Drake Passage. *Science*, **312**, 428-430.
- Ségalen, L., Renard, M., Lee-Thorp, J.A., Emmanuel, L., Le Callonnec, L., de Rafélis, M., Senut, B., Pickford, M. and Melice, J.-L. (2006). Neogene climate change and emergence of C_4 grasses in the Namib, southwestern Africa, as reflected in ratite ^{13}C and ^{18}O . *Earth and Planetary Science Letters*, **244**, 725-734.
- Sternberg, R. (1996). Workshop on secular variations in the rates of production of cosmogenic nuclides on Earth: Paleomagnetic averages of geomagnetic latitude. *Radiocarbon*, **38**, 169-170.
- Tankard, A.J., Jackson, M.P., Eriksson, K.A., Hobday, D.K., Hunter, D.R. and Minter, W.E.L. (1982). Crustal Evolution of Southern Africa: 3.8 Billion Years of Earth History, *Springer-Verlag, New York, United States of America*, 523pp.
- Tinker, J. (2005). Using apatite fission track thermochronology and offshore sedimentary volumes to test the balance between denudation (onshore) and deposition (offshore) since Gondwana break-up. *Unpublished Ph.D Thesis, University of Cape Town, South Africa*, 243pp.
- Tinker, J., de Wit, M.J. and Brown, R. (in review). Mesozoic uplift of southern Africa: using fission track thermochronology and offshore sediment volumes to test the balance between onshore denudation and offshore accumulation since Gondwana break-up. *Tectonophysics*.
- Tyson, P.D. and Partridge, T.C. (2000). Evolution of Cenozoic climates. In: T.C. Partridge and R.R. Maud (Editors) *The Cenozoic of Southern Africa, Oxford University Press, United Kingdom*, 371-387.
- Van der Wateren, F.M. and Dunai, T.J. (2001). Late Neogene passive margin denudation history – cosmogenic isotope measurements from the central Namib desert. *Global and Planetary Change*, **30**, 271-307.

Editorial handling: M. J. de Wit and Brian Horsfield